Original Paper

A High-speed Measurement System for Treadmill Spherical Motion in Virtual Reality for Mice and a Robust Rotation Axis Estimation Algorithm Based on Spherical Geometry

SATOSHI ZUGUCHI[1]   KAZUHIRO SAKAMOTO[1,2,a]   NORIHIRO KATAYAMA[3]   HAJIME MUSHIAKE[1]

Abstract: A head-fixed rodent virtual reality (VR) system allows imaging of neuronal activity from the brain during behavioral tasks. To accurately measure the complex two-dimensional behavior of animals, it is necessary to detect the motion of the spherical treadmill of the VR system with multiple sensors. However, commercial VR systems for rodents are not widely used; they are expensive and the algorithms used to calculate the motion of the spherical treadmill from sensor signals are not publicly available. We developed a system to detect the motion of a spherical treadmill at high-speed using two optical mice. The system can be used on a general-purpose VR platform. A novel algorithm to robustly calculate the rotation axis of the spherical treadmill using spherical geometry was also devised. This system enables accurate reconstruction of complex two-dimensional behaviors of animals. The system is open source, which should encourage the use of VR-based approaches for imaging brain activity in rodents during behavioral tasks.

Keywords: virtual reality system for rodents, open source, two optical mice, robust algorithm, spherical geometry

1. Introduction

Elucidating the functional structure of the brain is one of the major challenges of neuroscience. However, the brain is complex, and there is not always agreement as to what constitutes an understanding of the brain [1]. To clarify its function and structure, it is important that many scientists participate in brain research from various perspectives and using many methodologies, proposing diverse ideas and competitive results. To encourage scientists to enter the field of brain research, experimental platforms that are inexpensive and offer unique findings are needed.

The cerebral cortex, which plays a central role in the higher cognitive and behavioral functions in the brain, is divided into many functional structures or areas. However, not all areas have been well defined by classical anatomical studies (e.g., Ref. [2]). In several cases, what was previously thought to be one area has been distinguished as multiple areas upon appropriate experimentation [3], [4], [5]. For example, Broadman's area 6 was clearly divided into premotor and supplementary motor areas, only after recording neuronal activities in primates alternately performing visual- and memory-guided sequential movement tasks, which revealed the differences in the properties of the areas [3], [6]. However, identifying brain areas and mapping their functions using electrophysiological techniques alone is time consuming and labor intensive. For instance, a new area that Matsuzaka named the posterior medial prefrontal cortex required approximately 3,000 microelectrode penetrations to identify and accurately map the nature of the neural activity [5]. Moreover, some structures, such as the pinwheel structure in the primary visual cortex, are difficult to identify using electrophysiological techniques alone [7]. Therefore, novel imaging techniques are needed to facilitate more accurate cortical region identification and functional mapping.

In the field of neurophysiology, experiments using rodents, especially mice with various genetic modifications, are becoming increasingly important. In mice, it is possible to record cellular-level activity via two-photon imaging on a scale of several millimeters squared [8], [9]. Even without such high-end methods, imaging of endogenous signals is relatively cheap and simple and can successfully identify brain areas [10], [11]. For example, Tsukano et al. discovered new auditory areas in anesthetized mice via frequency response mapping based on flavin protein fluorescence imaging [12]. However, when attempting functional mapping of motor-related regions via imaging, it is essential to perform the mapping in animals under various appropriate conditions.

VR systems for mice are promising for functional brain mapping [13], [14], [15], [16], [17], which fulfill the seemingly contradictory requirements of head fixation for imaging and free behavior of the animal. In particular, when attempting to record brain activity associated with complex behaviors, a one-dimensional treadmill is not always sufficient. However, a spherical treadmill can accurately capture the two-dimensional motion of the animal on the spherical treadmill and link the stimulus pre-

---

[1] Department of Physiology, Tohoku University School of Medicine, Sendai, Miyagi 980–8575, Japan

[2] Department of Neuroscience, Faculty of Medicine, Tohoku Medical and Pharmaceutical University, Sendai, Miyagi 983–8536, Japan

[3] Shokei Gakuin College, Natori, Miyagi 981–1295, Japan

[a] sakamoto@tohoku-mpu.ac.jp

sentation with the motion [13], [14], [18], [19]. Spherical treadmill motion must be measured in at least three dimensions, since it is represented by the two-dimensional coordinates of the rotation axis and the one-dimensional angular velocity of rotation. A technique using two computer optical mice is the ideal option [13], [14], but commercially available VR systems for mice are too expensive for many research groups. Therefore, efforts are underway to develop platforms that provide advanced research resources for free or at low cost (e.g., in Japan [20]). Mushiake and Katayama, for instance, have supplied various technologies as part of such efforts [21]. To promote the use of mouse VR, resources for system construction should be provided as part of such platforms. However, the algorithms used to calculate the axis of rotation and angular velocity of rotation of a spherical treadmill using two computer optical mice have been described in detail and in only a few studies [22]. Algorithms must be able to accommodate commercially available optical mice, which differ in sensitivity and gain ("endogenous gain variation"), and allow reliable calculations of axes even when the distance between the optical mouse and spherical treadmill constantly changes due to animal movement on the latter ("exogenous gain variation"). Neither of these issues has been addressed in the literature.

Unity is the standard platform for building VR systems. While the availability of a variety of hardware and software on Windows makes it easy for researchers to build systems to suit their purposes, it is not possible to directly acquire sensor values from multiple optical mice on the Windows operating system. We therefore developed a communication library that can be plugged into Unity such that it acquires sensor values from multiple optical mice using the Windows Application Programming Interface (API). In addition, a novel algorithm that uses spherical geometry to calculate the rotation axis of the spherical treadmill robustly and in real time was devised, implemented, and included in the plug-in. By releasing the library as an open resource, researchers can build VR systems for rodents inexpensively and easily. Through these efforts, it is expected that rodent brain activity imaging using VR will become more widespread, and the functional structure of the brain will be elucidated further.

2. Methods

2.1 Setup of the VR System

A VR system for mice was constructed by attaching a second optical mouse to the system developed by Katayama et al. [23] (**Fig. 1**). The spherical treadmill (Hoyo Denshi Seiki, Sendai, Japan) mainly composed of a white spherical treadmill made of Styrofoam (radius = 10 cm, 70–85 g) and a bowl that holds the sphere and floats it with supplied air. The inner surface of the bowl is hemispherical and its upper edge is horizontal. The lower part of the bowl is connected to an oilless air compressor (OL-1525; UNITED, Osaka, Japan) by tubes with an inner diameter of 6 mm, which discharges air at a pressure of $\geq 2\,\mathrm{kgf/cm^2}$ and flow rate of $\geq 94\,\mathrm{L/min}$.

For simplicity, the stationary coordinates of the spherical treadmill are expressed below in latitude and longitude. The top of the spherical treadmill is the north pole, and the position of optical mouse 1 is 2° latitude and 0° longitude (hereinafter expressed as
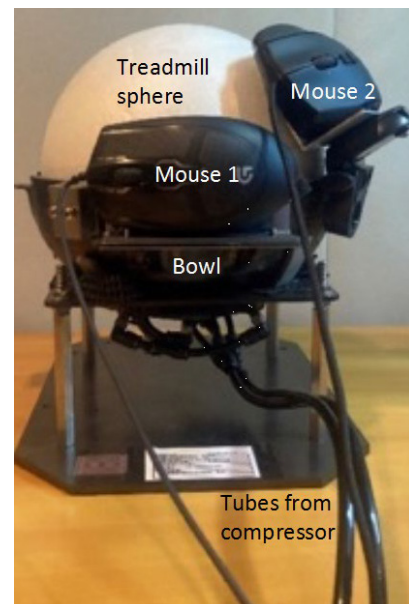

Fig. 1 Appearance of the spherical treadmill part of the 2-optical mice VR system for mouse. A white Styrofoam spherical treadmill is set in a black bowl.

(N2, EW0)). The circle forming the upper edge of the hemispherical bowl was aligned with the equatorial plane. Optical mouse 2 was placed at N23°, E57° (hereafter expressed as (N23, E57)). Both optical mice were positioned so that they were oriented parallel to the equator, and the positive directions the detected x and y values were the motion to the south and west of the spherical treadmill, respectively.

For reasons discussed below, the second optical mouse is intentionally moved out of the equatorial plane. Optical mice 1 (report rate = 500 Hz; G100S; Logitech, Lausanne, Switzerland) and 2 (G600; report rate = 1,000 Hz; Logitech) were connected to the computer via wired USB connections. The x and y axis gains of the two optical mice were set to DPI 250. The main specifications of the computer were as follows :

CPU: Core i7: 6850 K, 3.6 GHz, 15 MB, six-cores, 12 threads, 140 W

Memory: 32 GB (4×8 GB DDR4)

Graphics board: GeForce GTX1080: 8 GB GDDR5X. 4-screen output

OS: Windows 10 Pro: 64-bit DSP version

2.2 General Architecture for the Measurement of Treadmill Rotation

The communication library created in this study can be plugged into Unity to poll the RawInput Windows API based on requests for data acquisition from Unity. The library inquires whether or not optical mouse data are available in a fixed period of time, acquires those data, calculates the axis of rotation of the spherical treadmill and its rotation speed, etc., as necessary, and passes the results to Unity (**Fig. 2** A). In Windows, individual data items can be acquired from multiple optical mice using the RawInput API. To make VR applications available independent of the platform (Windows, MacOS, etc.), Unity interprets and executes scripts written mainly in the C# programming language. However, this makes it operationally difficult to access
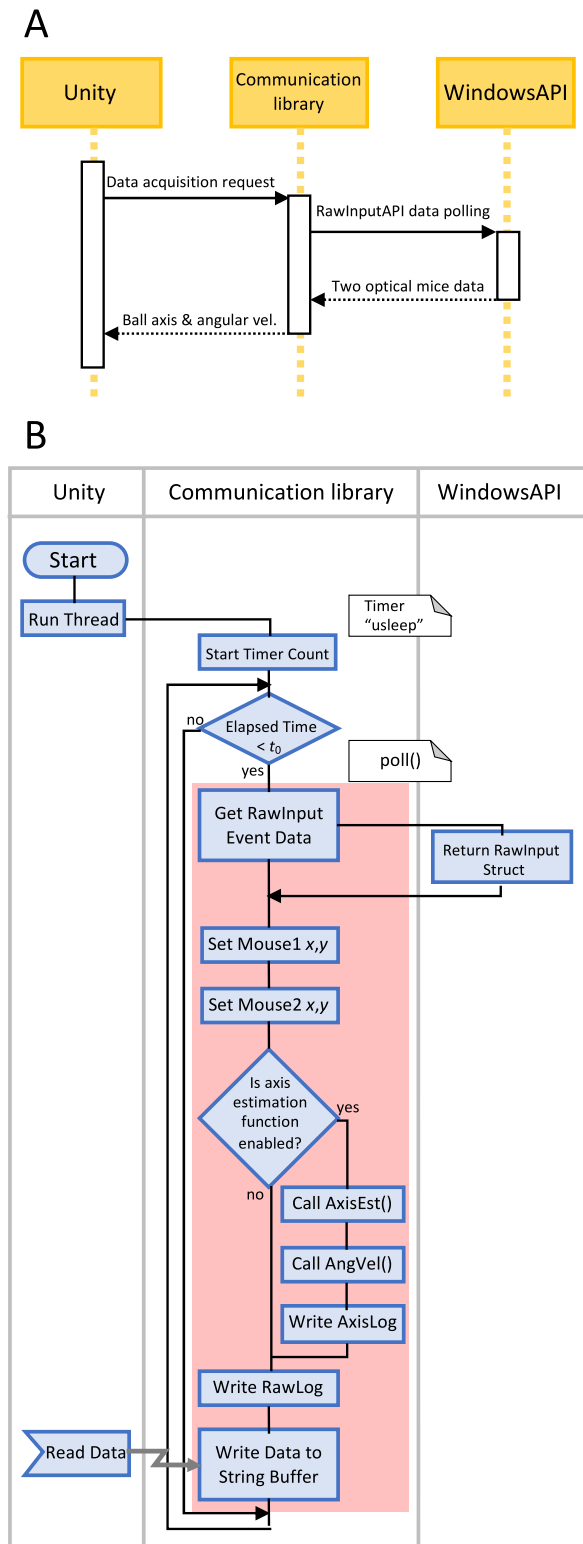
Fig. 2 System overview. A: Sequence diagram of the whole process. B: Flowchart of the process in the communication library, uni-morawi.dll.

Windows-specific RawInput API directly from Unity. Therefore, in this study, we used the C++ language as standard for accessing the Windows API and created a Dynamic Link Library (DLL). The signal processing results of the two optical mice were made available to Unity by plugging these features into it, which is a standard implementation scheme.

VR systems for rodents are used simultaneously with neural activity measurements of the animals in motion. To investigate the correspondence between behavior and neural activity, the optical mouse signal must be acquired with high temporal precision. Therefore, it is necessary to manage time more precisely than can be achieved with C# scripts. Also, because the temporal precision is higher than that normally required for computer games, communication libraries with the necessary precision are not available as open resources. Therefore, in this study, we constructed a new system that enables recording of the calling time of the polling function in the order of microseconds by using the std::chrono library of C++; the design was based on the latest C++ language standard {C++20-compliant}.

Details of the above process are shown in Fig. 2 B. A timer function, usleep (microsecond sleep), was created and interrupt processing was applied at specific time intervals to process the poll function (light red area in Fig. 2 B). Data for all events (displacement, click, wheel scroll, etc.) of all optical mice connected to the PC were acquired from RawInput API. Among the events, the poll function acquired both the value and time of the motion vector after the last poll detected by the target optical mouse. When enabled, the rotation axis and animal movement velocity vector calculation functions were performed, with the results recorded in the results log. The optical mouse ID, motion vector, and time were recorded by the poll function using this program, which could be referenced from the C# side by a marshalling process (conversion of the data into a format allowing exchange between programs). The poll function was embedded in the unimorawi.dll communication library (Unity-Mouse-RawInput). The library will be available on github.com, a source code management service that allows people around the world to store and publish program code and design data.

2.3   Calculation of Rotation Axis

Based on the signals of the two optical mice obtained as described above, the program calculates the axis of rotation and angular velocity of rotation of the spherical treadmill. To ensure that the created library can be offered as open source and thus widely used, it must be compatible with a variety of commercially available optical mice. The sensitivity of optical mice is not necessarily consistent among models, as some high-performance models allow independent adjustment of the x- and y-axis gain as needed. To ensure that the provided library is easy to use, its rotation axis calculation algorithm should not require estimation of the sensitivity of the optical mouse or gain adjustment, i.e., it should not depend on differences in endogenous gains. Furthermore, the distance between the spherical treadmill and optical mouse fluctuates constantly, albeit slightly, due to perturbation of the spherical treadmill caused by the animal's gait, etc. Thus, the detected values of the optical mouse can be expected to vary even when the spherical treadmill rotates in the same direction constantly. Therefore, the algorithm for calculating the axis of rotation of the spherical treadmill must be stable and unaffected by these exogenous gain changes, as well as by endogenous gain changes.

To satisfy the above two requirements, we developed and implemented a novel rotation axis calculation algorithm using
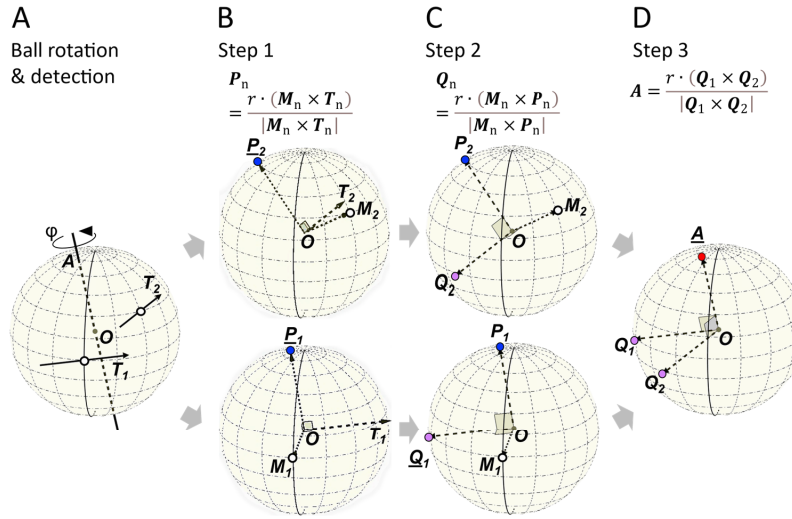
Fig. 3   Great circle method for calculating the axis of a rotating sphere. A: Rotation axis of the sphere A, rotation velocity φ, and tangent vectors of the motions T_n detected by the two optical mice. B: Vector P_n is obtained from the outer product of T_n and the position vector of the optical mouse M_n. C: The outer product of P_n and M_n yields the pole Q_n of the great circle on which A, rests. D: A is obtained from the outer product of Q_1 and Q_2. The vertical continuous line on the sphere represents "the prime meridian."

spherical geometry, i.e., the great circle method. The relationship between the great circle and pole on the sphere surface can be explained as follows. Consider a vector from the center of the sphere to any two points on the great circle; the vector obtained by the cross-product of the two vectors indicates the direction of the pole. This relationship is not only mathematically simple, but the reciprocal voting structure of the relationship between the great circle and poles in the parameter space allows the necessary information to be obtained robustly [1], [24], [25], [26], [27]. Moreover, the great circle algorithm used herein enables more robust calculation of the axis of rotation by using only the direction of the motion vectors detected by the two optical mice, which are gain-independent quantities.

Specifically, we first obtain the tangent vector T_n ($n = 1, 2$) of the motion by normalizing the motion vector V_n obtained from each optical mouse by its norm (**Fig. 3** A). This makes the following calculations independent of changes in endogenous and exogenous gains.

Let M_n be the position vector of each optical mouse with respect to the center O of the treadmill sphere (white circle in Fig. 3). Consider a vector extending from O by translating the tangent vector T_n of the motion. These normalized outer products (multiplied by the radius r of the spherical treadmill) are expressed as:

$$P_n = \frac{r \cdot (M_n \times T_n)}{|M_n \times T_n|}$$

(Fig. 3 B). P_n (Fig. 3, blue circle) is the vector representing the pole of the great circle containing the tangent vector T_n of the motion when T_n is attached to the position of each optical mouse (as in Fig. 3 A) (Step 1).

Next, the position vector of P_n and the optical mouse is calculated from the outer product of M_n as

$$Q_n = \frac{r \cdot (M_n \times P_n)}{|M_n \times P_n|}$$

(Fig. 3 C). This Q_n (Fig. 2 purple circle) is the pole of the great circle containing P_n and M_n, i.e., the pole of the great circle containing the rotation axis A (Fig. 2 red circle) (Step 2).

The axis of rotation A of interest is the intersection of the great circle with Q_1 as its pole and the great circle with Q_2 as its pole. Therefore, A is calculated as their outer product

$$A = \frac{r \cdot (Q_1 \times Q_2)}{|Q_1 \times Q_2|}$$

(Step 3; Fig. 3 D). Once A is obtained, the absolute value of the rotational angular velocity ω can be written as

$$|\omega| = \frac{|V_n|}{\sin(\cos^{-1}(A \cdot M_n))}.$$

In the special case in which Q_1 and Q_2 overlap, such as when the great circle containing the axis of rotation A estimated from the motion of each optical mouse overlaps, i.e., when the axis of rotation is on the great circle containing M_1 and M_2 (referred to herein as the "singular great circle"), A cannot be calculated correctly. In this case, the algorithm detects that the axis of rotation is in a singular great circle and computes it in a dedicated manner (Fig. A·1; see Appendix A.1). However, given that, in practice, animals often move in a straight line, it will often be the case that the axis of rotation is near the equatorial plane, i.e., around the rim of the bowl. In our system, the two optical mice were arranged so that they did not line up in the equatorial plane. With this arrangement, the singular great circle will rarely be a problem when estimating the axis of rotation for practical purposes.

The library also included a GetAx function that implemented the above great circle algorithm and a GetAxInv function that implemented the inverse matrix method (see Appendix A.2) [22], yielding the required value from among three values of the two velocity vectors by inversion. User can select whichever function they prefer.

2.4 Experiment to Evaluate the Treadmill-rotation Measurement System

To evaluate the data acquisition system based on two optical mice and algorithm for calculating spherical treadmill rotation described above, the spherical treadmill was rotated at various rotation axis angles. A step-out-less stepping motor (ASC46AK; ORIENTAL MOTOR Co., Ltd., Tokyo, Japan), controlled by an Arduino Uno-compatible machine with a CNC shield compatible with grbl 1.1, was used to rotate the sphere.

2.5 Statistical Evaluation of the Distribution of the Estimated Rotation Axes

To statistically evaluate whether the real rotation axes estimated from the optical mouse time series data are within a narrow range, we used the bootstrap method, as described below. Pseudo-x and -y time series data were generated by shuffling the time series of the x and y values of the optical mice, respectively, and the pseudo-rotation axes were calculated 10^6 times using these data. The data were then used to calculate the probability that the position of the pseudo-rotation axis was within the latitudinal and longitudinal maximum and minimum values of the real rotation axis position distribution. The same method was also used to evaluate the convergence of the angular distribution of the motion vectors measured by each optical mouse.

3. Results

The constructed system was capable of sampling optical mouse signals at a speed sufficient for practical use. **Figure 4** A, B shows examples of measured rotations of the spherical treadmill on the axis of rotation (N45, W90). In this example, sampling was done at an interval of 15 ms. Although sampling at 500 Hz (2 ms), which is the upper limit of the optical mouse report rate, was possible, a sampling rate of 15 ms was set as the default to obtain the largest and most stable optical mouse signal values possible, for practical use and to increase the calculation accuracy, based on a frame rate of the VR system screen of 60 Hz. Figure 4 C shows the sampling interval variability for the data in Fig. 4 A. Although there were a few 0.5-ms fluctuations during the 1.2 s of measurement, most were within the range of 15.0 ± 0.1 ms (mean $\pm$ SD: 15.00 ± 0.01 ms), which is considered acceptable for practical use.

The x and y values of each optical mouse at 0.2~0.8 s after the start of rotation (Fig. 4 A, B, shaded areas), when rotation was stable, were correlated (optical mouse 1, $r^2 = 0.98$, $n = 39$, $t = 41.3$, $p = 8.7 \times 10^{-34}$; optical mouse 2, $r^2 = 0.55$, $n = 39$, $t = 7.0$, $p = 2.3 \times 10^{-8}$: Fig. 4 D, E). Even when the spherical treadmill rotated at a constant speed, the optical mouse signals fluctuated to some extent due to subtle irregularities in the sphere surface. However, the correlation of the X and Y values shown in Fig. 4 D, E demonstrates that the tangent vector direction obtained from the signals of each optical mouse did not change significantly. This result validates the great circle method proposed in this study. In fact, the great circle method computed the axis of rotation very robustly, independent of slight fluctuations in signal values (N46.7 $\pm$ 0.3, W91.2 $\pm$ 1.1; bootstrap test, $p < 10^{-6}$, see Methods 2.5) (Fig. 4 F).
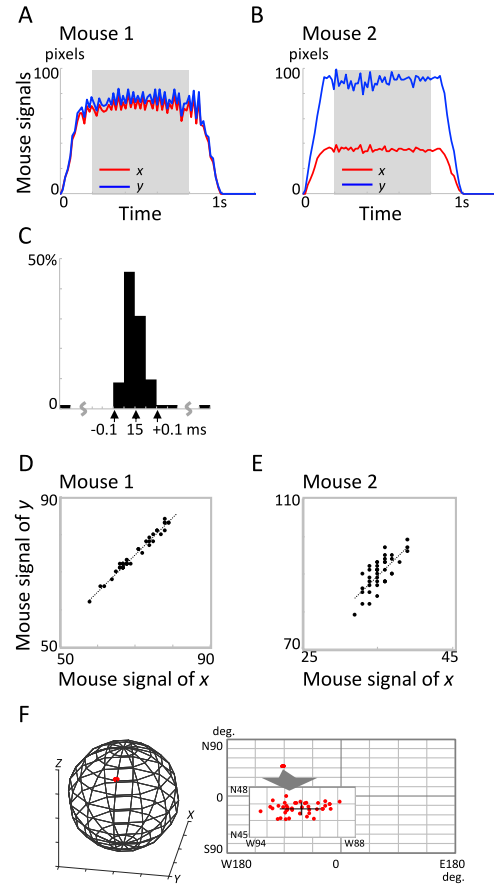

Fig. 4 Example of the measurement and axis calculations. A, B: Raw data from optical mice 1 (A) and 2 (B); the rotation axis was set at (N45, W90). Data in the shaded area between 0.2 and 0.8 s after the start of rotation are plotted in D, E, and F. C: Time interval accuracy of the data sampling; the rotation time was 1 s. D, E: Correlation between the x and y values of the motion vector detected by optical mice 1 (D) and 2 (E). F: The estimated axis of rotation of the spherical treadmill at each time point. Left, spherical plot. In this plot, $x > 0$, $x < 0$, $z > 0$, and $z < 0$ correspond to the eastern, western, northern, and southern hemispheres, respectively. Right, Mercator plot. Inset, magnified view near the estimated rotation axis.

The calculation was also stable even as the axis of rotation of the spherical treadmill varied: (North Pole), (N60, W90), (N60, E0), (N60, E90), (N60, E180), (N45, W90), (N45, E0), (N45, E90), (N45, E180), (N20, W90), (N20, E90), (N20, E180) are (N87.7 $\pm$ 1.2), (N60.6 $\pm$ 0.6, W80.2 $\pm$ 1.5), (N61.0 $\pm$ 0.8, E2.2 $\pm$ 1.3), (N57.3 $\pm$ 0.4, E90.1 $\pm$ 2.2), (N65.1 $\pm$ 1.2, E179.5 $\pm$ 1.2), (N46.7 $\pm$ 0.3, W91.2 $\pm$ 1.1), (N49.4 $\pm$ 0.6, W0.4 $\pm$ 0.8), (N44.0 $\pm$ 0.7, 89.8 $\pm$ 3.6), (N51.3 $\pm$ 1.3, E178.2 $\pm$ 1.9), (N20.9 $\pm$ 0.4, W90.7 $\pm$ 1.4), (N17.6 $\pm$ 0.5, E90.2 $\pm$ 2.6), (N19.5 $\pm$ 1.2, 179.4 $\pm$ 0.6), respectively (**Fig. 5**). In all cases, the axis calculations were extremely stable regardless of the fluctuation of the optical mouse signal: (bootstrap test: N60, W90, $p < 10^{-6}$; N60, E0, $p = 2.1 \times 10^{-5}$; N60, E90, $p < 10^{-6}$; N60, E180, $p < 10^{-6}$; N45, W90, $p < 10^{-6}$; N45, E0, $p < 10^{-6}$; N45, E90, $p < 10^{-6}$; N45, E180, $p < 10^{-6}$; N20, W90, $p < 10^{-6}$; N20, E90, $p < 10^{-6}$; N20, E180, $p < 10^{-6}$). The obtained rotation axis positions also revealed the average absolute values of the differences from the target latitude and longitude (2.4 $\pm$ 1.9 and 1.6 $\pm$ 2.8, respectively); these values were sufficient considering that the accuracy of the experimental rotation axis setting was limited to approximately $\pm$ 5° at low latitudes.
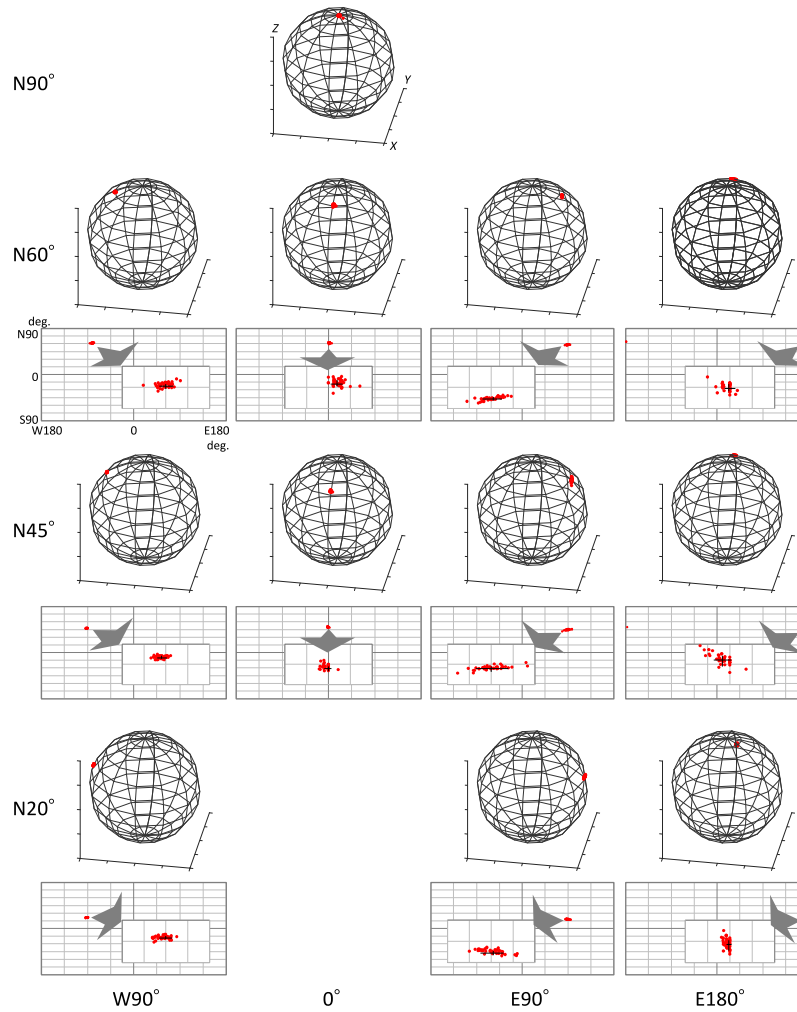
Fig. 5 Estimated axes of rotation of the spherical treadmill at various rotation axes. The data intervals used to analyze were as in Fig. 4 F. Note that the spherical plot is rotated 90° to the west from Fig. 4 F. In this plot, $x > 0$, $x < 0$, $z > 0$, and $z < 0$ correspond to the eastern, western, northern, and southern hemispheres, respectively. Inset, magnified view near the estimated rotation axis. Scale is 5°.

The relative gains of the two optical mice can vary. Exogenous gain changes can arise, for example, due to fluctuations in optical mouse signals resulting from fluctuations in reflected light, such as those caused by changes in the position of the spherical treadmill due to an animal walking, etc. Endogenous gain variation can occur due to differences in model and gain settings. The robustness of the two optical mice against such relative gain changes was examined in this study by expanding (150%) and contracting (50%) the signal value of optical mouse 2 (**Fig. 6**). The great circle method proposed in this study was then compared with a naive method, i.e., the inverse matrix method [22] (Appendix A.2) for the example used in Fig. 4 (N45, W90). When neither was scaled up or down, the two methods calculated the same rotation axis (Fig. 6 B, E). Since the great circle method obtains tangent vectors by ignoring the norms of the motion vectors detected in each optical mouse, it produced exactly the same axis calculation values when the signal values of optical mouse 2 were reduced (Fig. 6 A) or expanded (Fig. 6 C) (N46.7 ± 0.3, W91.2 ± 1.1). By contrast, in the inverse matrix method, which uses the motion vector values directly, a drift in the calculated axis positions occurred as they were reduced or expanded (50%:

N45.7 ± 0.4, W109.2 ± 1.2), (100%: N46.8 ± 0.3, W92.7 ± 2.6), (150%: N45.2 ± 0.5, W75.8 ± 3.6) (Fig. 6 D, F). These means and SDs are summarized in Fig. 6 G to show the differences in the estimated rotation axis positions.

In experiments that primarily assume forward motion of the animal, a system using a single optical mouse is used to detect the spherical treadmill motion [28]. Since the information obtained from a single optical mouse is two-dimensional, the rotational motion of the spherical treadmill, which is represented in three dimensions, cannot be accurately obtained. Therefore, the assumption that the axis of rotation is on the equatorial plane is used [23]. **Figure 7** shows how the motion of an animal assumed to be placed at the North Pole is calculated using the one-optical-mouse method. The rotation of the spherical treadmill when the animal is moving forward (toward the date line) is clockwise to the axis (N0, W90). Including this case, when the axes of rotation are on the W90 line, the motion vector at the north pole is always in the direction of the date line, as calculated using the great circle method, and the amplitude decreases as the latitude of the rotation axis increases. If we denote the angle and amplitude combination of the motion vector in the case of
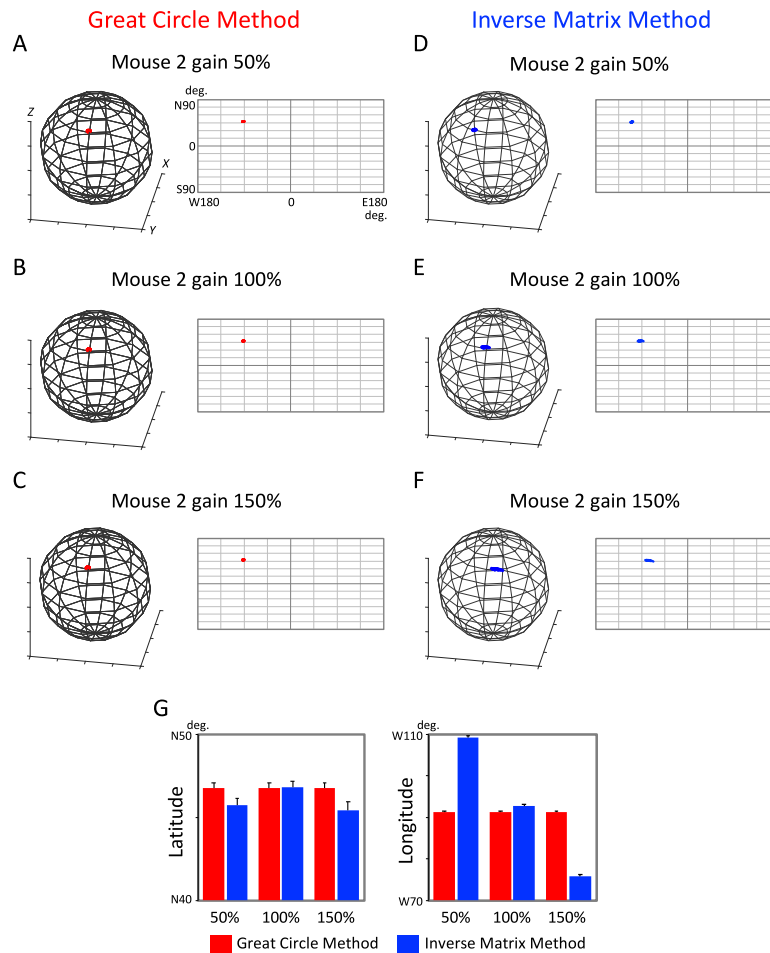
Fig. 6 A–F: Example comparison of the axis calculation between the great circle method (A–C) and the inverse matrix method (D–F). Plots for optical mouse 2 gain: 50% (A, D), 100% (B, E), 150% (C, F). The data and format used are the same as in Fig. 4 F; that is, Fig. 6 B is identical to Fig. 4 F except for the inset. In the spherical plot, $x > 0$, $x < 0$, $z > 0$, and $z < 0$ correspond to the eastern, western, northern, and southern hemispheres, respectively. G: The mean ± SD of the computed rotation axes. Left, latitude. Right, longitude.
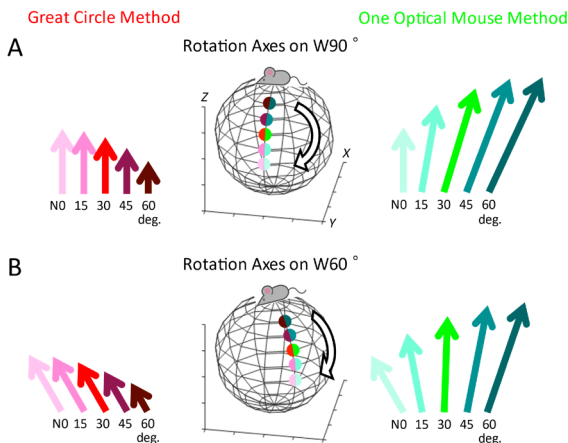

Fig. 7 Examples of estimated motion vectors at the North Pole. A: Rotation axes on the W90 line. B: Axes on the W60 line. Left column, motion vectors estimated using the great circle method. Right column, motion vectors estimated using the one-optical-mouse method. Arrows, motion vectors. The upward direction is straight ahead, i.e., motion in the opposite direction of optical mouse 1.

(N0, W90) as (0.0°, 1.00), then (N15, W90), (N30, W90), (N45, W90), and (N60, W90) are (0.0°, 0.97), (0.0°, 0.87), (0.0°, 71), and (0.0°, 0.50), respectively (Fig. 7 A, left). The one-optical-

mouse method correctly calculates the motion vector for (N0, W90) as (0.0°, 1.00); however, as the latitude of the rotation axis increases, the calculated motion vectors for (N15, W90), (N30, W90), (N45, W90), and (N60, W90) are (−10.3°, 0.97), (−16.5°, 0.97), (−21.0°, 0.87), and (−24.9°, 0.71), respectively (Fig. 7 A, right), which is highly inaccurate. That is, when the latitude of the rotation axis is greater than 0, the calculated direction shows rightward rotation when the actual rotation is to the left, and the calculated amplitude increases when the actual amplitude decreases. A similar trend is observed when the axes of rotation are at W60 (Fig. 7 B). When the axis of rotation is on the equator, both methods can accurately calculate the motion vector at the North Pole as (30.0°, 1.00). As the latitude of the rotation axis increases to (N15, W60), (N30, W60), (N45, W60), and (N60, W60), the actual motion vectors are (30.0°, 0.97), (30.0°, 0.87), (30.0°, 0.71), and (30.0°, 0.50), respectively (Fig. 7 B, left); however, the one-optical-mouse method yields values of (11.1°, 1.24), (−1.5°, 1.48), (−10.8°, 1.67), and (−18.5°, 1.78), respectively (Fig. 7 B, right).

The optical mouse data used until this point were sampled at 15 ms. The motion vectors detected for optical mice 1 and 2 when sampled at 2 ms are shown in **Fig. 8** A and B, respectively. Com-
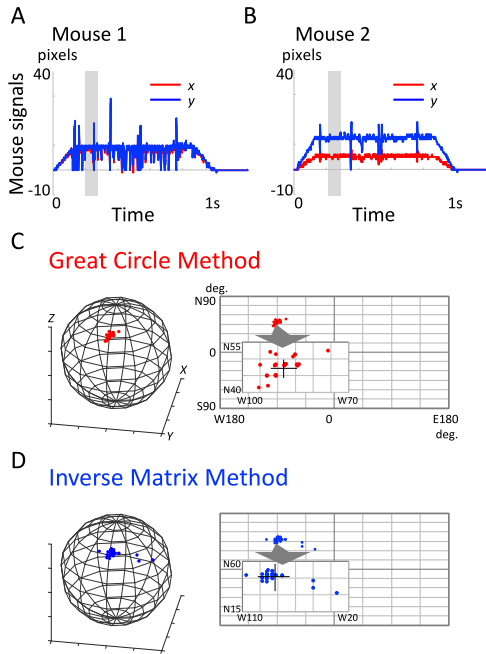
Fig. 8 Example of the measurement and axis calculation using the 2-ms sampling data. A, B. Raw data from optical mice 1 (A) and 2 (B). The rotation axis was set at (N45, W90). The rotation time was 1 s. Data in the shaded area 0.2–0.28 s after the start of rotation are plotted in C and D and match the number of data points in Fig. 4. C. The estimated rotation axis at each time point calculated using the great circle method. D. The same plot obtained using the inverse matrix method. Left, spherical plot. In this plot, $x > 0$, $x < 0$, $z > 0$, and $z < 0$ correspond to the eastern, western, northern, and southern hemispheres, respectively. Right, Mercator plot. Inset, magnified view near the estimated rotation axis.

pared with Fig. 4 A and B, the x and y values for each mouse were not only smaller, while maintaining a larger and smaller relationship, but also showed larger variability. Reflecting this, the results of the rotation axis estimation were (N88.9 ± 3.6, W47.4 ± 2.5), and the latitudinal and longitudinal SDs were 3.3 and 7.4 times larger, respectively, than those in the 15-ms sampling case (Fig. 8 B). However, the inverse matrix method yielded an estimated axis of rotation of (N84.4 ± 12.9, W46.7 ± 3.7), with latitudinal and longitudinal SDs 11.8 and 10.9 times larger, respectively, than those of the great circle method obtained with 15-ms sampling. Thus, the great circle method provides good estimates of the rotation axes of the spherical treadmill.

4. Discussion

In this study, we constructed a system to acquire the rotation of a spherical treadmill at high speed in mouse VR using two optical mice connected to a Windows device. A newly developed great circle method was then used to calculate the sphere rotation axis robustly. The constructed system achieved a sufficiently fast signal acquisition time for practical use. In a comparison with the conventional method, the proposed great circle method computed the axis of rotation more robustly in various experimental situations. The open source availability of the multiple optical mouse signal processing library will encourage measurements of brain activity in behaving animals, thereby further elucidating brain function under conditions in which local and global neural activities strongly interact.

In our study, a program that accesses RawInputAPI, a Windows API, was implemented to acquire signals from multiple optical mice at high speed. Sampling was possible even at 500 Hz (2 ms), which is the upper limit of the reported rate of the optical mice used, but the signal values were smaller in that case. To obtain the largest and most stable optical mouse signal values possible, the default sampling rate was set to 15 ms (67 Hz). The time scale of Ca^{2+} transient [28], [29], [30], [31], [32] and flavin fluorescence [10], [11], [33], [34] signals are approximately 1 s. Hence, the imaging frame rate of systems that perform Ca^{2+} imaging during VR is much slower than 67 Hz and does not exceed 16 Hz (64 ms) [14], [16]. In addition, the refresh rate of the video projection system (HC3000; Mitsubishi, Tokyo, Japan) used in those VR systems is approximately 60 Hz [15], [35]. Thus, we foresee no major problems with defaulting to acquiring the optical mouse signal at a report rate of 15 ms (67 Hz), which is faster than those of the previous systems. Moreover, our system can handle the fastest report rate of 2 ms for an optical mouse, which should compensate for any issues.

We also proposed a novel algorithm to robustly calculate the sphere rotation axis. The proposed great circle algorithm was superior to the naive inverse matrix method, in that the former can robustly compute the axis of rotation regardless of differences in the gain of individual optical mice and the variations in signal values caused by small changes in the distance between the spherical treadmill and optical mouse due to animal movement, etc. (Fig. 6). Nonetheless, our method has a larger range of singularities that are more difficult to calculate than when using the inverse matrix method. That is, it has a singular great circle that passes through the positions of the two optical mice, in which case the rotation axis cannot be uniquely determined. To address this problem, we devised an algorithm that detects the axis of rotation on a singular great circle and then performs another process (Fig. A·1; see Appendix A.1), and did not align the two optical mice on the equator of the spherical treadmill. The latter measure was feasible given that, in the VR environment, animals often move in a straight line, i.e., the axis of rotation is often in the equatorial plane. Our robust method for calculating the axis of rotation can be expected to reduce the need for fine-tuning custom-made VR systems developed for small animals, while yielding data with less variability.

A commercially available mouse VR system that uses two optical mice can be found in Refs. [13], [36], [37]. However, one study [13] offered no description, and another study [37] provided only the brief description that "Ball rotations around the mediolateral axis were used for forward and backward movement along the running direction of the mouse, whereas ball rotations around the anteroposterior and dorsoventral axes were used in combination to change the mouse's running direction." Therefore, the existing literature does not clarify the details of the calculation of treadmill motion. We presume that the existing approach does not calculate the rotation axis of the spherical treadmill, as in our method and the inverse matrix method; thus, that system is unlikely to evaluate the rotational motion accurately.

The most common use of VR systems for mice is imaging neural activity during navigation [15], [16], [38], [39], [40], in which

case usage of a single optical mouse is possible [16]. However, robust, accurate estimation of the rotation of a spherical treadmill using two optical mice, as in this study, would greatly expand the range of experiments possible. As examples, we can consider adaptive learning [41], [42], [43], which has a long history of research, and predictive coding [44], [45], which has become a topic of interest in recent years. Prism adaptation, as it has long been known, is an adaptive learning phenomenon in which the task is to perform reaching movements under conditions in which the visual environment is modulated by prism glasses. While the subject initially fails to reach the target, he or she eventually becomes able to do so. Since prism adaptation does not occur in patients with cerebellar disease, the cerebellum has been thought to play an important role in this adaptive learning, i.e., comparison of the obtained visual image with the outcome predicted by movement and adaptive modification of the movement [46], [47], [48]. In recent years, more modern theories [44], [45] and experimental techniques [49], [50] have led to the idea that modulation is caused by active prediction and its errors in wide areas of the brain [51], [52], [53], [54]. For example, Kim et al. observed changes in cellular activities when the VR gain (i.e., the ratio of the mouse's forward motion to the associated visual image shift) was abruptly changed to produce a mismatch between predicted and actual VR motion, and they confirmed that midbrain dopamine cell activity encoded the time difference signal [55]. The accurate measurement of two-dimensional animal motion proposed in this study could be used to conduct a wider range of experiments on predictive coding. For example, it is possible to verify the effect of rotation rate modulation on locomotion, such as walking in a straight line while showing a gentle left curve in the VR environment. Furthermore, unlike prisms, the correspondence between stimulus and motion can be continuously modulated, and the degree of adaptive learning quantified. With the development of more realistic VR systems, including the inclusion of tactile sensation [17] and force sensation [56], a broader range of experiments will be possible.

The capability to present a variety of paths one after another is another advantage of the VR system that is not possible in experiments using real devices. For example, if a mouse learns a visually guided right rotation → left rotation → right rotation sequence, and then the visual cue is removed, can the mouse quickly perform the same sequence guided by memory? Also, do mice show changes in cortical activities from premotor to supplementary motor areas similar to those observed in monkeys [3]? By detecting these changes, can novel areas be identified in mice? Can mice perform different sequential behaviors one after another? Even if they cannot switch behaviors like monkeys, how long does it take them to learn? To address this last question in particular, using our system to accurately measure motion during rotation, it is possible to quantify the predictive behavior associated with learning to evaluate whether the mouse overshoots and rotates when learning has not progressed or, conversely, whether the mouse rotates smoothly when learning has progressed.

Although artificial neural networks have attracted public attention in recent years, it is a major mission of experimental neuroscience to show that they still differ substantially from the actual brain, especially in terms of the highly complex functional structure of the brain. For example, the primary visual cortex of primates has a functional structure (or retinotopy) that corresponds to locations in the visual field, in addition to other functional maps of modalities such as ocular dominance, color, orientation of contours, and spatial frequency [57], [58]. In other words, the primary visual cortex has high-dimensional maps embedded in its three-dimensional structure. If each area of the cortex has common properties, it is not unreasonable to assume that other areas, especially motor-related areas, also have such higher dimensional maps. The involvement of many researchers and efficient functional mapping is essential to reveal such complex functional structures. To this end, relatively inexpensive and simple methods such as endogenous signal imaging that can easily map functions over a few millimeters squared, as well as VR systems that enable imaging during animal movement, are indispensable. Contributions by many research groups to the construction of inexpensive, simple mouse VR systems will promote brain research and help elucidate the functional structure of the brain.

References

[1] Sakamoto, K.: *Brain Science of Creativity: Beyond the Complex Systems Theory of Biological Systems*, University Tokyo Press, Tokyo (2019).
[2] Brodmann, K.: *Vergleichende Lokalisationslehre der Grosshirnrinde*, Johann Ambrosius Barth, Leipzig (1909).
[3] Mushiake, H., Inase, M. and Tanji, J.: Neuronal Activity in the Primate Premotor, Supplementary, and Precentral Motor Cortex during Visually Guided and Internally Determined Sequential Movements, *J. Neurophysiol.*, Vol.66, pp.705–718 (1991).
[4] Mastuzaka, Y., Aizawa, H. and Tanji, J.: A Motor Area Rostral to the Supplementary Motor Area (Presupplementary Motor Area) in the Monkey: Neuronal Activity during a Learned Motor Task, *J. Neurophysiol.*, Vol.68, pp.653–662 (1992).
[5] Matsuzaka, Y., Akiyama, T., Tanji, J. and Mushiake, H.: Neuronal Activity in the Primate Dorsomedial Prefrontal Cortex Contributes to Strategic Selection of Response Tactics, *Proc. Natl. Acad. Sci. U.S.A.*, Vol.109, pp.4633–4638 (2012).
[6] Shima, K., Tanji, J.: Neuronal Activity in the Supplementary and Presupplementary Motor Areas for Temporal Organization of Multiple Movements, *J. Neurophysiol.*, Vol.84, pp.2148–2160 (2000).
[7] Bonhoeffer, T. and Grinvald, A.: Iso-Orientation Domains in Cat Visual Cortex are Arranged in Pinwheel-Like Patterns, *Nature*, Vol.353, pp.429–431 (1991).
[8] Ota, K., Oisi, Y., Suzuki, T., Ikeda, M., Ito, Y., Ito, T., Uwamori, H., Kobayashi, K., Kobayashi, M., Odagawa, M., Matsubara, C., Kuroiwa, Y., Horikoshi, M., Matsushita, J., Hioki, H., Ohkura, M., Nakai, J., Oizumi, M., Miyawaki, A., Aonishi, T., Ode, T. and Murayama, M.: Fast, Cell-Resolution, Contiguous-Wide Two-Photon Imaging to Reveal Functional Network Architectures across Multi-Modal Cortical Areas, *Neuron*, Vol.109, pp.1810–1824 (2021).
[9] Yu, C.H., Stirman, J.N., Yu, Y., Hira, R. and Smith, S.L.: Diesel2p Mesoscope with Dual Independent Scan Engines for Flexible Capture of Dynamics in Distributed Neural Circuitry, *Nat. Communications*, Vol.12, 6639 (2021).
[10] Shibuki, K., Hishida, R., Murakami, H., Kudoh, M., Kawaguchi, T., Watanabe, M., Watanabe, S., Kouuchi, T. and Tanaka, R.: Dynamic Imaging of Somatosensory Cortical Activities in the Rat Visualized by Flavoprotein Autofluorescence, *J. Physiol. (Lond.)*, Vol.549, pp.919–927 (2003).
[11] Yanagawa, Y., Takasu, K., Osanai, H. and Tateno, T.: Salicylate-

Induced Fre-quency-Map Reorganization in Four Subfields of the Mouse Auditory Cortex, *Hearing Res.*, Vol.351, 98e115 (2017).

[12] Tsukano, H, Horie, M., Hishida, H., Takahashi, K., Takebayashi, H. and Shibuki, K.: Quantitative Map of Multiple Auditory Cortical Regions with a Stereotaxic Fine-Scale Atlas of the Mouse Brain, *Sci. Reports*, Vol.6, 22315 (2016).

[13] Hölscher, C., Schnee, A., Dahmen, H., Setia, L. and Mallot, H.A.: Rats are Able to Navigate in Virtual Environments, *J. Exp. Biol.*, Vol.208, No.3, pp.561–569 (2005).

[14] Dombeck, D.A., Khabbaz, A.N., Collman, F., Adelman, T.L. and Tank, D.W.: Imaging Large-Scale Neural Activity with Cellular Resolution in Awake, Mobile Mice, *Neuron*, Vol.56, No.1, pp.43–57 (2007).

[15] Harvey, C.D., Collman, F., Dombeck, D.A. and Tank, D.W.: Intracellular Dynamics of Hippocampal Place Cells During Virtual Navigation, *Nature*, Vol.461, No.7266, pp.941–946 (2009).

[16] Dombeck, D.A., Harvey, C.D., Tian, L., Looger, L.L. and Tank, D.W.: Functional Imaging of Hippocampal Place Cells at Cellular Resolution During Virtual Navigation, *Nat. Neurosci.*, Vol.13, No.11, pp.1433–1440 (2010).

[17] Sofroniew, N.J., Cohen, J.D., Lee, A.K. and Svoboda, K.: Natural Whisker-Guided Behavior by Head-Fixed Mice in Tactile Virtual Reality, *J. Neurosci.*, Vol.34, No.29, pp.9537–9550 (2014).

[18] Seelig, J.D., Chiappe, M.E., Lott, G.K., Dutta, A., Osborne, J.E., Reiser, M.B. and Jayaraman, V.: Two-Photon Calcium Imaging from Head-Fixed, *Drosophila* during Optomotor Walking Behavior, *Nature Methods*, Vol.7, No.6, pp.535–540 (2010).

[19] Moore, R.J.D., Taylor, G.J., Paulk, A.C., Pearson, T., van Swinderen, B. and Srinivasan, M.V.: FicTrac: A Visual Method for Tracking Spherical Motion and Generating Fictive Animal Paths, *J. Neurosci. Methods*, Vol.225, pp.106–119 (2014).

[20] available from ⟨http://model.umin.jp⟩.

[21] available from ⟨https://www.lbc.mech.tohoku.ac.jp/physio-sien/⟩.

[22] Lee, K-M. and Zhou, D.: A Real-Time Optical Sensor for Simultaneous Measurement of Three-DOF Motions, *IEEE/ASME Trans. Mechatronics.*, Vol.9, No.3, pp.499–507 (2014).

[23] Katayama, N., Hidaka, K., Karashima, A. and Nakao, M.: Development of an Immersive Virtual Reality System for Mice, *Proc. SICE Annu. Conf.*, pp.791–794 (2012).

[24] Sugie, Y., Kawakami, S., Sakamoto, K. and Yano, M.: A Cell Model for Detecting the Time-to-Passage of a Line, *Annu. Conf. Jpn. Neu. Netw. Soc.*, P2–08 (2006).

[25] Sakamoto, K., Ohori, A., Sugie, Y., Sasaki, H., Kawakami, S. and Yano, M.: A Model for Shape Vision in the Cortical Area V4 Using Great Circle/Small Circle Transformation, *Annu. Conf. Jpn. Neu. Netw. Soc.*, P1–06 (2006).

[26] Sakamoto, K., Kohama, T., Sugie, Y., Kawakami, S., Hashimoto, M. and Yano, M.: An Area CIP Model Presuming the 3D Surface Orientation of a Line Drawing using Polar Transformation, *Annu. Conf. Jpn. Neu. Netw. Soc.*, P3–02 (2008).

[27] Sakamoto, K., Kumada, T. and Yano, M.: A Computational Model that Enables Global Amodal Completion Based on V4 Neurons, *Lec. Note Comput Sci.*, Vol.6443, pp.9–16 (2010).

[28] Rajasethupathy, P., Sankaran, S., Marshel, J.H., Kim, C.K., Ferenczi, Lee, S.Y., Berndt, A., Ramakrishnan, C., Jaffe, A., Lo, M., Liston, C. and Deisseroth, K.: Projections from Neocortex Mediate Top-Down Control of Memory Retrieval, *Nature*, Vol.526, pp.653–659 (2015).

[29] Tallini, Y.N., Ohkura, M., Choi, B.R., Ji, G., Imoto, K., Doran, R., Lee, J., Plan, P., Wilson, J., Xin, H.B., Sanbe, A., Gulick, J., Mathai, J., Robbins, J., Salama, G., Nakai, J. and Kotlikoff, M.I.: Imaging Cellular Signals in the Heart In Vivo: Cardiac Expression of the High-Signal Ca^{2+} Indicator GCaMP2, *Proc. Natl. Acad. Sci. U.S.A.*, Vol.103, pp.4753–4758 (2006).

[30] Ohkura, M., Sasaki, T., Kobayashi, C., Ikegaya, Y. and Nakai, J.: An Improved Genetically Encoded Red Fluorescent Ca^{2+} Indicator for Detecting Optically Evoked Action Potentials, *PLoS One*, Vol.7, e39933 (2012).

[31] Ohkura, M., Sasaki, T., Sadakari, J., Gengyo-Ando, K., Kagawa-Nagamura, Y., Kobayashi, C., Ikeaya, Y. and Nakai, J.: Genetically Encoded Green Fluorescent Ca2+ Indicators with Improved Detectability for Neuronal Ca2+ Signals, *PLoS One*, Vol.7, e51286 (2012).

[32] Chen, T.W., Wardill, T.J., Sun, Y., Pulver, S.R., Renninger, S.L., Baohan, A., Schreiter, E.R., Kerr, R.A., Orger, M.B., Jayaraman, V., Looger, L.L., Svoboda, K. and Kim, D.S.: Ultrasensitive Fluorescent Proteins for Imaging Neuronal Activity, *Nature*, Vol.499, pp.295–300 (2013).

[33] Honma, Y., Tsukano, H., Horie, M., Ohshima, S., Tohmi, M., Kubota, Y., Takahashi, K., Hishida, R., Takahashi, S. and Shibuki, K.: Auditory Cortical Areas Activated by Slow Frequency-Modulated Sounds in Mice, *PLoS One*, Vol.8, e68113 (2013).

[34] Baba, H., Tsukano, H., Hishida, R., Takahashi, K., Horii, A., Takahashi, S. and Shibuki, K.: Auditory Cortical Field Coding Long-Lasting Tonal Offsets in Mice, *Sci. Reports*, Vol.6, 34421 (2016).

[35] available from ⟨https://dl.mitsubishielectric.co.jp/dl/ldg/wink/ssl/wink_doc/m_contents/ wink/D_MENT_DOC/manual_hc3000.pdf⟩.

[36] available from ⟨https://www.phenosys.com/products/virtual-reality/jetball-tft/?cn-reload ed=1⟩.

[37] Schmidt-Hieber, C. and Häusser, M.: Cellular Mechanisms of Spatial Navigation in the Medial Entorhinal Cortex, *Nat. Neurosci.*, Vol.16, pp.325–331 (2013).

[38] Harvey, C.D., Coen, P. and Tank, D.W.: Choice-Specific Sequences in Parietal Cortex During a Virtual-Navigation Decision Task, *Nature*, Vol.484, pp.62–68 (2012).

[39] Aghajan, Z.M., Acharya, L., Moore, J.J., Cushman, J.D., Vuong, C. and Mehta, M.R.: Impaired Spatial Selectivity and Intact Phase Precession in Two-Dimensional Virtual Reality, *Nat. Neurosci.*, Vol.18, pp.121–128 (2015).

[40] Driscoll, L.N., Pettit, N.L., Minderer, M., Chettih, S.N. and Harvey, C.D.: Dynamic Reorganization of Neuronal Activity Patterns in Parietal Cortex, *Cell*, Vol.170, pp.986–999 (2017).

[41] Marr, D.: A Theory of Cerebellar Cortex, *J. Physiol. (Lond.)*, Vol.202, pp.437–470 (1969).

[42] Ito, M.: Neurophysiological Aspects of the Cerebellar Motor Control System, *Intl. J. Neurol.*, Vol.7, pp.162–176 (1970).

[43] Albus, J.S.: A Theory of Cerebellar Functions, *Math. Biosci.*, Vol.10, pp.25–61 (1971).

[44] Friston, K.: A Theory of Cortical Responses, *Philos. Trans. R. Soc. Lond. B Biol. Sci.*, Vol.360, pp.815–836 (2005).

[45] Keller, G.B. and Mrsic-Flogel, T.D.: Predictive Processing: A Canonical Cortical Computation, *Neuron*, Vol.100, pp.424–435 (2018).

[46] Weiner, M.J., Hallett, M. and Funkenstein, H.H.: Adaptation to Lateral Displacement of Vision in Patients with Lesions of the Central Nervous System, *Neurol.*, Vol.33, pp.766–772 (1983).

[47] Martin, T.A., Keating, J.G., Goodkin, H.P., Bastian, A.J. and Thach, W.T.: Throwing while Looking through Prisms I. Focal Olivocerebellar Lesions Impair Adaptation, *Brain*, Vol.119, pp.1183–1198 (1996).

[48] Baizer, J.S., Kralj-Hans, I. and Glickstein, M.: Cerebellar Lesions and Prism Adaptation in Macaque Monkeys, *J. Neurophysiol.*, Vol.81, pp.1960–1965 (1999).

[49] Huang, K.H., Rupprecht, P., Frank, T., Kawakami, K., Bouwmeester, T. and Friedrich, R.W.: A Virtual Reality System to Analyze Neural Activity and Behavior in Adult Zebrafish, *Nat. Methods*, Vol.17, pp.343–351 (2020).

[50] Torigoe, M., Islam, T., Kakinuma, H., Fung, C.C.A., Isomura, T., Shimazaki, H., Aoki, T., Fukai, T. and Okamoto, H.: Zebrafish Capable of Generating Future State Prediction Error Show Improved Active Avoidance Behavior in Virtual Reality, *Nat. Communications*, Vol.12, 5712 (2021).

[51] Taylor, J.A. and Ivry, R.B.: Cerebellar and Prefrontal Cortex Contributions to Adaptation, Strategies, and Reinforcement Learning, *Prog. Brain Res.*, Vol.210, pp.217–253 (2014).

[52] McDougle, S.D., Ivry, R.B. and Taylor, J.A.: Taking Aim at the Cognitive Side of Learning in Sensorimotor Adaptation Tasks, *Trends Cogn. Sci.*, Vol.20, No.7, 535–544 (2016).

[53] Panico, F., Fleury, L., Trojano, L. and Rossetti, Y.: Prism Adaptation in M1, *J. Cogn. Neurosci.*, Vol.33, No.4, pp.563–573 (2020).

[54] Panico, F., Rossetti, Y. and Trojano, L.: On the Mechanisms Underlying Prism Adaptation: A Review of Neuro-Imaging and Neuro-Stimulation Studies, *Cortex*, Vol.123, pp.57–71 (2020).

[55] Kim, H.G.R., Malik, A.N., Mikhael, J.G., Bech, P., Tsutsui-Kimura, I., Sun, F., Zhang, Y., Li, Y., Watabe-Uchida, M., Gershman, S.J. and Uchida, N.: A Unified Framework for Dopamine Signals across Timescales, *Cell*, Vol.183, pp.1600–1616 (2020).

[56] Katayama, N., Nakao, M., Tanaka, T., Osanai, M. and Mushiake, H.: Multimodal Functional Analysis Platform: 3. Spherical Treadmill System for Small Animals in Optogenetics, *Adv. Exp. Med. Biol.*, Yawo, H., Kandori, H., Koizumi, A. and Kageyama, R. (Eds.), Vol.1293, pp.493–500 (2021).

[57] Livingstone, M.S. and Hubel, D.H.: Anatomy and Physiology of a Color System in the Primate Visual Cortex, *J. Neurosci.*, Vol.4, pp.309–356 (1984).

[58] Hubel, D.H.: *Eye, Brain, and Vision*, Scientific American Library, New York (1983).

Appendix

A.1 Algorithm Applied when the Axis of Rotation is on the Singular Great Circle

If the axis of rotation is on the great circle containing M_1 and M_2 (referred to herein as the "singular great circle"); that is, if Q_1 and Q_2 in Fig. 3 overlap, the axis of rotation cannot be calculated correctly. In this case, specifically, if Q_1 and Q_2 are very close to each other and below a threshold value, the axis of rotation is considered to be on the singular great circle, and the algorithm shown in the Supplementary Figure is used to calculate the axis of rotation A.

Let S_1, S_2 and E_1, E_2 be the vectors from the sphere center of the start and endpoints of the motion vectors detected by the two optical mice, respectively. The axis of rotation A is the intersection of the great circles passing through S_1 and S_2, and through E_1 and E_2 (**Fig. A·1**). Then, the poles of each great circle are obtained as

$$U_1 = \frac{r \cdot (S_1 \times S_2)}{|S_1 \times S_2|}$$
$$U_2 = \frac{r \cdot (E_1 \times E_2)}{|E_1 \times E_2|}$$

(Fig. A·1 B). Since the pole of the great circle passing through these two poles is the axis of rotation of interest, we obtain the vector of A from the outer product

$$Ax = \frac{r \cdot (U_2 \times U_1)}{|U_2 \times U_1|}$$

(Fig. A·1 C). The algorithm depends on the norm of the motion vector. However, considering that, in the VR environment, animals often move straight ahead, i.e., the axis of rotation meets the equatorial plane more frequently, the exception that applies to
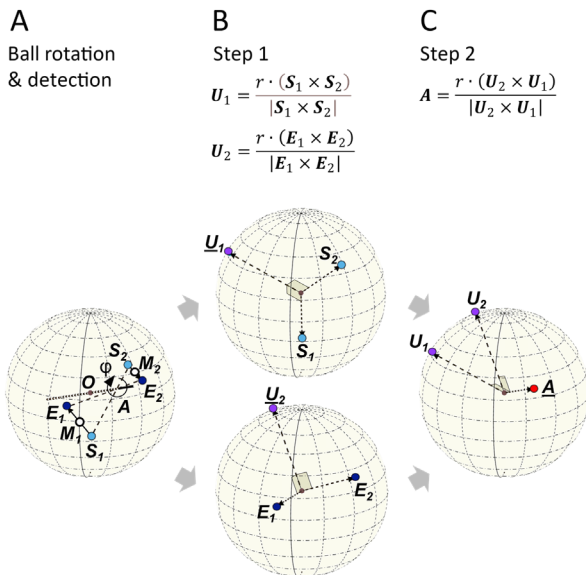
this singular great circle will arise less frequently, if the two optical mice are placed so that they are not aligned with the equator of the spherical treadmill. As a result, the axis of rotation can in fact be calculated robustly.

A.2 Rotation Axis Calculation Using Inverse Matrix Method

The positions of the axis of rotation and optical mouse n ($n = 1$ or 2) on the spherical treadmill are represented by vectors A and M_n from the sphere center O, respectively (Fig. 3 A). When the directions of the north pole of the sphere and optical mouse 1 are set to the Z- and X-axes, respectively, M_n is expressed in polar coordinates as

$$M_n = r \begin{pmatrix} \cos\varphi_n \sin\vartheta_n \\ \sin\varphi_n \sin\vartheta_n \\ \cos\vartheta_n \end{pmatrix},$$

where φ_n and θ_n are the angles that the vector makes with the Z- and X-axes, respectively, and r is the radius of the spherical treadmill. A can also be expressed as a similar three-dimensional vector. The motion vector $v_n = (v_{xn}, v_{yn})^T$ detected by the optical mouse n can then be obtained from A, while the 2×3 matrix can be expressed as

$$v_n = \omega \begin{pmatrix} -\cos\varphi_n \sin\vartheta_n & -\sin\varphi_n \cos\vartheta_n & \sin\vartheta_n \\ \sin\varphi_n & -\cos\varphi_n & 0 \end{pmatrix} A,$$

where ω is the angular velocity of rotation.

Since the position vector on the sphere, including A, is three-dimensional, A can be obtained from the inverse of the 3×3 matrix using three values of four motion vector variables $(v_{x1}, v_{y1})^T$, $(v_{x2}, v_{y2})^T$ detected by the two optical mice [8]. Specifically, to simplify the calculation, we used v_{x1}, v_{y1}, v_{y2} so that the 3×3 matrix contains many zero elements, i.e.,

$$x_0 =$$
$$\begin{pmatrix} 0 & -\cos\varphi_2 \sin\vartheta_1 \\ 0 & -\sin\varphi_2 \sin\vartheta_1 \\ \cos\varphi_1 \sin\varphi_2 - \sin\varphi_1 \cos\varphi_2 & -(\cos\varphi_1 \cos\varphi_2 + \sin\varphi_1 \sin\varphi_2)\cos\vartheta_1 \end{pmatrix}$$

$$\begin{pmatrix} \cos\varphi_1 \sin\vartheta_1 \\ \sin\varphi_1 \sin\vartheta_1 \\ \cos\vartheta_1 \end{pmatrix} \begin{pmatrix} v_{x_1} \\ v_{y_1} \\ v_{y_2} \end{pmatrix},$$

and obtained A as

$$A = r \frac{x_0}{|x_0|}.$$

A Ball rotation & detection
B Step 1
$$U_1 = \frac{r \cdot (S_1 \times S_2)}{|S_1 \times S_2|}$$
$$U_2 = \frac{r \cdot (E_1 \times E_2)}{|E_1 \times E_2|}$$
C Step 2
$$A = \frac{r \cdot (U_2 \times U_1)}{|U_2 \times U_1|}$$

Fig. A·1   Process of axis of rotation estimation for a singular great circle. A: The rotation axis of the sphere A, rotation velocity φ, position vector of the optical mice M_1, M_2, and start points S_1, S_2 and endpoints E_1, E_2 of the motion vector detected by each mouse. B: The pole U_1 corresponding to the start points S_1, S_2 on the great circle, and the pole U_2 corresponding to the endpoints E_1, E_2 on the great circle. C: The axis of rotation A is obtained from the outer product of U_1 and U_2.

Satoshi Zuguchi M.D. was born in 1988. He is a fourth-year doctoral graduate student in the Tohoku University Graduate School of Medicine. He graduated from Asahikawa Medical University with a Bachelor of Medicine in March 2014. His research interests include systems neuroscience and bioinformatics.

Kazuhiro Sakamoto was born in 1968. He received his B.S. and M.S. from the University of Tokyo in 1991 and 1993, respectively. He became a research associate and assistant professor at Tohoku University in 1993 and 2007, respectively. He received his Ph.D. from Tohoku University in 2009. He became an associate professor at Tohoku Medical and Pharmaceutical University in 2016. His research interests include neurophysiology, complex systems theory and neural networks. He is a member of the JNSS, PSJ, IPSJ and SfN, and a governing board member of JNNS.

Norihiro Katayama was born in 1967. He received his B.E., M.E., and Ph.D. from Tohoku University in 1991, 1993, and 1996, respectively. He became a research associate, an associate professor at Tohoku University in 1996 and 2003, respectively. He has been a professor at Shokei Gakuin University since 2022. His research interests include neuroscience, virtual reality, and biomedical engineering. He is a member of the IEEE, VRSJ, SICE, and JSMBE.

Hajime Mushiake was born in 1958. He received M.D. and Ph.D. from graduated Tohoku University School of medicine in 1987. He became a research associate in Department of Physiology in Tohoku University, in 1987–1989 a postdoctoral fellow in the State University of New York in Syracuse under supervisory of Dr. Peter Strick in 1989–1993, a research associate in Department of Physiology in Tohoku University in 1993–1996, an associative professor in Department of Physiology in Tohoku University in 1997, a professor in Department of Physiology in Tohoku University since 2005.

(Communicated by *Junichiro Yoshimoto*)